Tuning gold nanostar morphology for the SERS detection of uranyl

Rachel A. Harder,[1] Lahiru A. Wijenayaka,[1,2] Hoa T. Phan,[1] and Amanda J. Haes[*,1]

[1]University of Iowa, Department of Chemistry, Iowa City, Iowa USA
[2]Current Address: Department of Chemistry, The Open University of Sri Lanka, Nawala, 11222, Sri Lanka

[*]**Correspondence**
Amanda J. Haes, University of Iowa, Department of Chemistry, Iowa City, Iowa, 52242 USA
Email: amanda-haes@uiowa.edu

ABSTRACT

The impact of tunable morphologies and plasmonic properties of gold nanostars are evaluated for the surface enhanced Raman scattering (SERS) detection of uranyl. To do so, gold nanostars are synthesized with varying concentrations of the Good's buffer reagent, 2-[4-(2-hydroxyethyl)-1-piperazinyl]propanesulfonic acid (EPPS). EPPS plays three roles including as a reducing agent for nanostar nucleation and growth, as a nanostar-stabilizing agent for solution phase stability, and as a coordinating ligand for the capture of uranyl. The resulting nanostructures exhibit localized surface plasmon resonance (LSPR) spectra that contain two visible and one near-infrared plasmonic modes. All three optical features arise from synergistic coupling between the nanostar core and branches. The tunability of these optical resonances are correlated with nanostar morphology through careful transmission electron microscopy (TEM) analysis. As the EPPS concentration used during synthesis increases, both the length and aspect ratio of the branches increase. This causes the two lower energy extinction features to grow in magnitude and become ideal for the SERS detection of uranyl. Finally, uranyl binds to the gold nanostar surface directly and via sulfonate coordination. Changes in the uranyl signal are directly correlated to the plasmonic properties associated with the nanostar branches. Overall, this work highlights the synergistic importance of nanostar morphology and plasmonic properties for the SERS detection of small molecules.

KEYWORDS

SERS, nanostars, morphology, uranyl, LSPR

1 | INTRODUCTION

The lightning rod or antenna effect associated with anisotropic nanostructures such as gold nanostars make these materials ideal for substrates in surface enhanced Raman scattering (SERS). Previously, it was shown that cubes,[1] triangles,[2,3] rods,[4-8] tetrapods,[9] and spiked nanostructures (i.e., nanostars)[8,10-12] are superior substrates for SERS because of the large electromagnetic fields that arise at the near-field of structural features with small radii of curvature. Gold nanostars, for instance, were previously shown to exhibit large electromagnetic fields near the sharp tips at the ends of their branches. These fields, which decay exponentially tens of nanometers from the tip surface,[13] have enabled a range of applications including highly

sensitive LSPR sensing,[14] SERS,[15] biomedicine,[16] and thermosplasmonics.[17] For instance, individual gold nanostars were shown to promote SERS enhancements up to 10^7 without aggregation or resonance Raman effects.[18] This signal enhancement was attributed to molecules localized at the nanostar tips where the electric field strengths are largest,[18] making gold nanostars a promising architecture in surface enhanced spectroscopies.

Key to designing effective SERS substrates is the generation of materials with ideal optical properties that promote plasmonic enhancement. To achieve these effects, synthetic strategies that systematically tune the morphology and as a result, the plasmonic properties are then utilized. Previously, it was shown that the localized surface plasmon resonance (LSPR) of SERS substrates can be tuned into the near infrared (NIR) or even the mid infrared (MIR) regions of the electromagnetic spectrum via anisotropic morphologies such as nanotriangles,[19] nanoantennas,[20] nanostars,[21-23] and tetrapods.[24] These structures allow for low energy excitation so that sample heating and decomposition can be minimized while also facilitating large electric field generation without the need of particle-particle coupling.

SERS also relies on the ability of a molecule to interact within these large electric fields for at least the duration of the SERS measurement.[25,26] This is often promoted via surface chemistry. For instance, we previously used gold nanostars functionalized with a carboxylate-terminated alkanethiol to promote the detection of uranyl (uranium (VI) oxide, UO_2^{2+}).[27,28] In these studies, the uranyl cation formed a covalent coordinate bond with the carboxylate species on gold nanostars. SERS signals followed Langmuir-like behavior and depended on the length of the alkane chain where shorter chains yielded the largest SERS responses.

Herein, a seedless, one-step synthesis is used to yield gold nanostars with tunable plasmon resonances and morphologies. This straightforward synthesis yields gold nanostars with up to three extinction features. These materials remain stable for prolonged periods when stored in an EPPS solution. Upon rinsing and dispersion in acidified water, the SERS detection of uranyl with nanostars with tunable morphologies is evaluated. Morphology features including branch length and aspect ratio are shown to be important in supporting ideal plasmonic properties for SERS detection. All in all, systematic correlation between nanostar morphology and SERS detection of uranyl is demonstrated. The novelty of this study include use of inherent rather than carboxylated surface chemistry to promote uranyl detection, evaluation of nanostar morphology on plasmon enhancement of uranyl, and excitation of dark plasmon modes to maximize SERS enhancement. While the interaction is weak, the sulfonate group in EPPS serves to bind uranyl to the nanostar surface for successful SERS detection. Importantly, the plasmon tunability and plasmonic coupling between nanostar branches on a single nanostar results in easily detectable and reproducible SERS signals for uranyl.

2 | EXPERIMENTAL METHODS

2.1 Gold nanostar synthesis

Gold nanostars were synthesized using $HAuCl_4$ and 2-[4-(2-hydroxyethyl)-1-piperazinyl]propanesulfonic acid (EPPS) via a one-step, solution-phase redox chemistry reaction, where EPPS acts as the buffer as well as the reducing agent.[9] All glassware were cleaned with

Aqua Regia ($HCl:HNO_3$ in a 3:1 ratio by volume) and rinsed with Nanopure water. A 1 M stock solution of EPPS was prepared in Nanopure water (initial pH ~5.9), and the pH was adjusted to 7.4 ± 0.1 at 25 °C with 1 M NaOH. This resulted in an 850 mM EPPS stock solution. Next, 5 mL aliquots of this stock were diluted using water so that the final EPPS concentrations ranged from 20 – 400 mM. Finally, 50 µL of 20 mM $HAuCl_4$ solution was added to each solution followed by gentle swirling of the glass reaction vessel. The solutions were equilibrated overnight to ensure gold nanostar formation. After 12-18 hours, the nanostars were centrifuged at 2000xg for 30 minutes in decreasing EPPS concentration to a final concentration of 5 mM then stored. Prior to use, the nanostars were centrifuged using identical conditions then suspended into water.

2.2 Optical and structural characterization

LSPR spectra were collected using an UV-VIS-NIR spectrometer (i-trometer, B&W Tek). Spectral ranges collected using different spectrometers were combined at 1000 nm and a scaling factor applied to account for detector response differences. Measurements were collected in transmission geometry and PMMA cuvettes with a 0.5 cm pathlength. Extinction maximum wavelength values were determined using zero point crossing values of the first derivatives in these spectra. Gold nanostar concentrations were determined using previously published extinction coefficients.[29] These values are 1.37, 2.24, 3.17, and 3.90×10^9 $M^{-1}cm^{-1}$ for nanostars synthesized using 20, 50, 100, and 400 mM EPPS, respectively. LSPR spectra were calculated before and after uranyl addition to ensure that the optical properties of the nanostars did not change significantly. Experimental conditions were optimized so that the low energy visible extinction maximum wavelength ($\lambda_{max,2}$) did not shift more than 3 nm throughout the experiment (see Fig. 1).

Gold nanostars were characterized using a transmission electron microscope (TEM, JEOL 1230) equipped with a Gatan CCD camera. Samples were prepared by first diluting the nanoparticle solution by 50% using ethanol. Next, this solution was pipetted onto 400 mesh copper grids coated with a thin film of Formvar and carbon (Ted Pella). TEM images were analysed (Image Pro Analyzer or Image J) to estimate the tip-to-tip dimensions (max, min, mean of an object), diameter, projected area, branch length (core to tip), radius of curvature of the tips (determined using the Three Point Circular ROI plugin), and aspect ratio (branch length/2*radius of curvature). Each image was calibrated using their respective scale bar. At least seven images were analyzed per sample. All data within 2σ were included in this structural analysis.

2.3 SERS measurements and analysis

SERS measurements were performed using Au nanostars diluted in water to an optical density of 0.6 at $\lambda_{max,2}$ and 40 µM uranyl nitrate. A 10 mM uranyl stock solution was used in these studies. Small aliquots of this solution were added to gold nanostar solutions that had been equilibrated for 5 minutes at pH 3 (adjusted using HNO_3).[30] Solution pH was measured using pH paper (Whatman, England) and was 3-4 for all measurements. Samples were vortexed for 10 seconds then allowed to equilibrate for 10 minutes. Prior to SERS analysis, samples were vortexed briefly then analyzed using a semi-homebuilt Raman microscope (ExamineR 785 spectrometer (DeltaNu)) with an excitation wavelength (λ_{ex}) of 785 nm, power = 35 mW, integration time (t_{int}) = 15 seconds, and 5 averages. These collection parameters and excitation wavelength were

selected to minimize sample heating and plasmonic losses. Raw data were treated by subtracting a control measurement (concentration matched gold nanostar solutions without uranyl) from a uranyl containing sample.

Vibrational spectra were analyzed in the uranyl window (900-750 cm^{-1}).[31,32] Vibrational band deconvolution was performed using Origin Pro 2018 and Gaussian functions. Second derivative analysis was used by analyzing first and second derivative spectra as previously demonstrated.[30] Deconvolution was performed if a vibrational feature was greater than 6 times the standard deviation (σ) of a Gaussian band or if the full width at half maximum (Γ) exceeded ~2.355*σ. For the SERS spectral features observed here, these values ranged from ~20-30 cm^{-1}, consistent with the literature.[33] Vibrational features were deconvoluted by applying the Savitzky-Golay filtering function (8-12 points) and second order polynomial analysis. A second derivative was calculated, and all wavenumbers that exceeded a 20% threshold were considered significant. These centers were then used for Gaussian function analysis. Restrictions in band centers (±2 cm^{-1}), Γ (18-32 cm^{-1}), S/N>3, and a minimum tolerance fitting error of 10^{-6} with positive magnitudes are reported. Noise was calculated from the standard deviation of a spectrum from 1850-1950 cm^{-1}. Measurements were performed in at least triplicate.

3 | RESULTS AND DISCUSSION

3.1 Optical characterization of gold nanostars

SERS intensities depend on the plasmonic properties of metallic nanostructures, which are related to their structure and composition.[23,34] In this study, branched gold nanostructures or nanostars are used as SERS substrates because their complex architecture gives rise to LSPR features that can be tuned by controlling the diameter of the core particle as well as the length and density of the protruding branches.[13,35] As shown in Fig. 1, the optical properties of 0.5 nM gold nanostars synthesized using varying EPPS concentrations exhibit tunable LSPR spectra. To collect these data, nanostars were centrifuged then dispersed in water until 0.5 nM concentrations were achieved. Previously published extinction coefficients were used to determine concentration.[29] It is important to note that the nanostars did not show signs of aggregation, and the spectral features remain consistent with the originally synthesized materials.

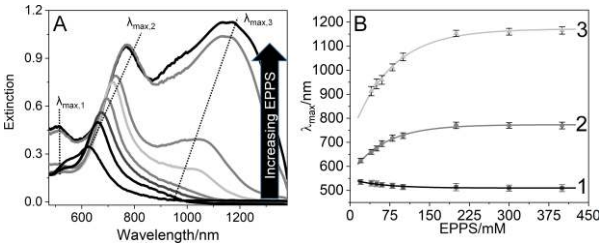

Figure 1. LSPR (A) spectra and (B) analysis of 0.5 nM gold nanostars synthesized in the presence of 20-400 mM EPPS at (1) $\lambda_{max,1}$, (2) $\lambda_{max,2}$, and (3), $\lambda_{max,3}$. After cleaning, samples were diluted in water prior to analysis.

As shown in Fig. 1A, three plasmonic features are observed for nanostars synthesized using EPPS. Consistent with prior studies,[23] the plasmonic properties of nanostars can be understood in terms of morphology, which consists of spherical as well as elongated (nanorod-like) architectures thus giving rise to multiple plasmon resonance features. The anisotropic optical properties of gold nanostars exhibit LSPR spectral features that are strongly dependent on the size (i.e., length and width) of the branches.[36,37]

Two of the plasmonic features are located in the visible region of the electromagnetic spectrum. The first λ_{max} ($\lambda_{max,1}$) is observed at wavelengths less 550 nm. This band blue shifts slightly as the concentration of EPPS used increases (Fig. 1B-1). The second feature ($\lambda_{max,2}$) is larger in magnitude and lower in energy than the first. As shown in Fig. 1B-2 this band red shifts with increasing EPPS concentration. Previously, these two plasmonic features were described using a hybridization model.[13] The highest energy feature is attributed to an anti-bonding plasmon mode and largely dependent on the plasmonic properties of the nanostar cores. The lower energy mode ($\lambda_{max,2}$) is attributed to a bonding plasmon feature with significant contributions from the nanostar branches and finite contributions from its core.[13] As nanostar branch length increases, the degree of hybridization between the core and branch plasmons increase. This causes the energy-level splitting between the bonding and anti-bonding plasmon modes to also increase in magnitude.[13] This enhanced hybridization, thus, gives rise to a red shift in the λ_{max} of the bonding plasmon feature and a slight blue shift in the anti-bonding mode.

Although the visible plasmonic properties of gold nanostars are well studied, fewer investigations of their near infrared resonances have been reported.[23,36,38] As shown in Fig. 1, a NIR plasmonic feature is observed in these spectra as well. This wavelength ($\lambda_{max,3}$) red shifts from 900-1150 nm, grows in magnitude, and becomes the largest spectral feature as EPPS concentration increases to 400 mM. Previously, this feature was predicted using discrete dipole approximation calculations and attributed to electromagnetic coupling between branches on a single nanostar,[39] a phenomenon that should be more probable as branch length on the nanostars increase. This suggests that gold nanostar branch length increases with increasing EPPS concentration.

3.2 Correlation of optical properties to nanostar structure

The plasmonic features observed in Fig. 1 are consistent with branched nanostructures and nanostars that are structurally anisotropic. This is important because higher order plasmon features are known to enhance the intensity of dark plasmon modes,[40] an attribute that can be exploited in SERS.[41,42] In order to observe and quantify morphological variations caused by changing EPPS concentration during synthesis, select samples of gold nanostars were imaged using transmission electron microscopy (TEM). As shown in Fig. 2, increasing EPPS concentration during nanostar nucleation and growth leads to the formation of branched nanostructures with increasing branch lengths (Fig. 2A). Nanostructures synthesized using 20, 50, 100, and 400 mM EPPS are shown because these exhibit clear structural

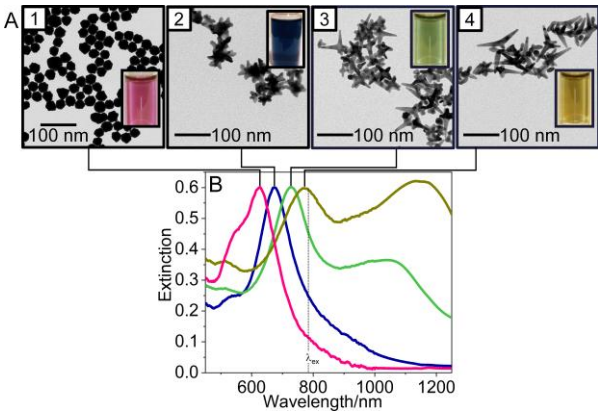

Figure 2. Representative (A) TEM images (photos insets) and (B) LSPR spectra of gold nanostars synthesized using (1) 20, (2) 50, (3) 100, and (4) 400 mM EPPS. Samples were rinsed and dispersed into water prior to analysis until an optical density of 0.6 was achieved. Nanostar concentrations are 0.87, 0.54, 0.38, and 0.31 nM, respectively.

variations, solution colors (insets), and tunable plasmonic properties (Fig. 2B).

The TEM data show systematic variations in the impact of EPPS concentration on gold nanostar morphology. For instance, each nanostructure is non-spherical and contains 3 to 5 branches (or bumps for the lowest EPPS concentration). This is consistent with prior literature results where Good's buffers such as HEPES resulted in predominantly branched tetrapod nanostructures.[24] With the exception of the nanostructures synthesized using the lowest EPPS concentration, nanostar core dimensions are similar (6-8 nm in diameter), but the branch lengths systematically increase. This is consistent with correlated LSPR spectra, which suggest that anisotropic or directional growth of nanostar branches occurs with increased EEPS concentration used during nanostar growth.

To evaluate these morphology changes more closely, nanostar structure was quantified through TEM analysis. In particular, gold nanostar diameter (largest dimension through the center of an object), radius of curvature of the branch tips, branch length, and average aspect ratio of the branches (approximated from the branch length divided by two times the radius of curvature of the branch tips) are analyzed. These results are shown in Fig. 3. Because these structures are three-dimensional with branches pointing in many directions, only measurement that fall within a 95% confidence interval of the mean value are included. The actual ranges are indicated with asterisks in each of the panels in Fig. 3.

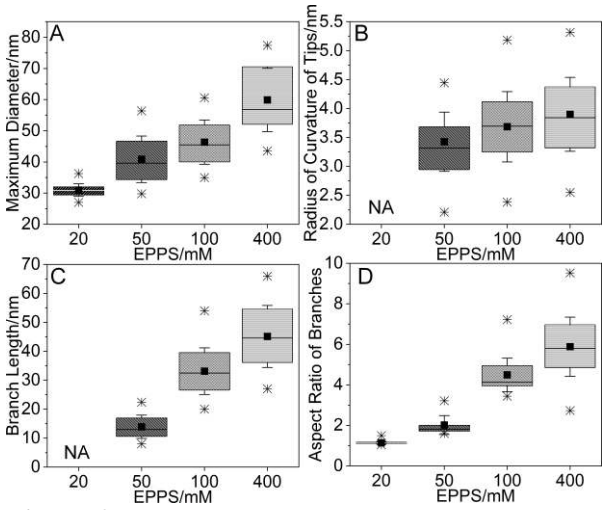

Figure 3. Structural analysis of gold nanostars as a function of (A) maximum diameter, (B) radius of curvature of the tips, (C) branch length, and (D) aspect ratio of the branches. Box and whisker plots were generated by calculating the mean (square) and standard deviation (error bars) and first, middle, and third quartiles. The asterisks indicate the data points observed with two standard deviations of the mean. At least 100 measurements were used.

While the nanostars clearly exhibit some degree of structural heterogeneity, clear trends are observed. In all cases, structural distributions as indicated by the box and whisker plots in Fig. 3, show that each dimension increases on average as the EPPS concentration used during synthesis increases. For instance, the overall size as indicated by the maximum diameter observed increases with increasing EPPS concentration. These vary from 31.0±2.0 (median 30.9 nm) to 59.9±10.2 nm (median 56.9 nm) over the EPPS concentration ranges studied. Projected two-dimensional areas increase similarly (data not shown). These values are 630, 660, 750, and 950 nm^2, respectively. For structures synthesized using the lowest EPPS concentration, the structures are more raspberry-like than star-like; however, all other nanostructures exhibit clear branching. For those three samples (EPPS concentrations 50-400 mM), the nanostar branches were analyzed with respect to radius of curvature of the branch tips and branch length (Fig. 3B and 3C, respectively). The radius of curvature increases slightly from 3.4±0.5 to 3.9±0.6 nm for nanostars prepared with increasing EPPS concentrations.

Structural changes that are more significant are observed in branch length. Because samples prepared using 20 mM EPPS contained ill-defined branches, these were not analyzed here. For the other three samples, branch length increased from 13.9±4.0 to 33.1±8.0 to 45.1±10.7 nm for nanostars prepared in 50, 100, and 400 mM EPPS, respectively. This increase in branch length is consistent with changes in the low energy visible plasmon resonance observed in Fig. 1 and 2. In each case, the relative standard deviation in branch length varies by ~25% suggesting that branch growth is occurring uniformly among the various samples.

Finally, the average aspect ratio of the structures are analyzed given the importance of aspect ratio in SERS.[43] These data are summarized in Fig. 3D. The aspect ratio for the entire nanostructure is calculated for samples prepared using 20 mM EPPS while aspect ratio is calculated for the nanostar branches in all other samples. Aspect ratio increases from 1.1±0.1, 2.0±0.5, 4.5±0.8, and 5.9±1.5 for the four EPPS concentrations studied. This result is consistent with LSPR data and the formation of the NIR plasmonic feature.[37] Furthermore, this structural component will be shown to be important for SERS applications (*vide infra*).

3.3 SERS detection of uranyl using tunable gold nanostars

The tunable plasmonic properties and sharp features inherent in gold nanostar morphology make them ideal candidates as SERS substrates. Previously, gold nanostars synthesized using Good's buffers were shown to exhibit SERS activity upon equilibration at pH 3-4 to weaken the affinity of the sulfonate group and protonate one of the nitrogen atoms in the piperazine group in EPPS.[30] As shown in Fig. 4A, this activation step changes the electron distribution in the surface stabilizing agent, weakening its overall affinity, and exposing the gold surface for possible small molecule adsorption.

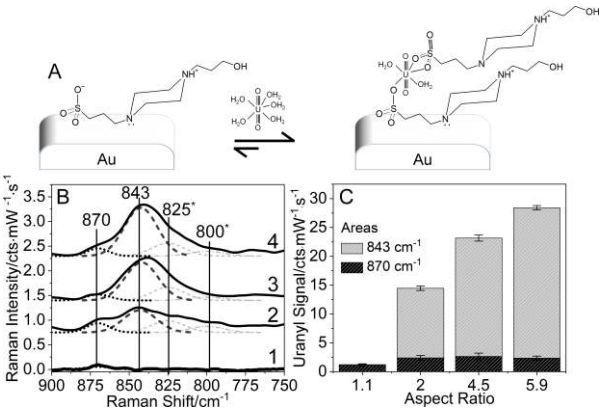

Figure 4. SERS detection of uranyl using gold nanostars. (A) Schematic of uranyl binding to gold nanostars. (B) Representative SERS spectra of 40 μM uranyl (pH 3-4) using gold nanostars with an optical density of 0.6 and aspect ratios of (1) 1.1, (2) 2.0, (3) 4.5, and (4) 5.9. These were rinsed and redispersed in water that contains some residual EPPS. Samples were incubated for 10 minutes then analyzed. A 2-3 nm shift in $\lambda_{max,2}$ were observed in the extinction spectra. Two uranyl species are detected via direct adsorption to Au (870 cm^{-1}) and via sulphonate coordination (843 cm^{-1}). Two additional vibrational modes are observed at 825 and 800 cm^{-1} and are assigned to EPPS. (C) Trends in total uranyl signal as a function of EPPS concentration. SERS experimental conditions: λ_{ex} = 785 nm, t_{int} = 15 s, P = 35 mW, averages = 5.

In this study, we use the small molecule uranyl because of its inherently large Raman cross section associated with the U-O symmetric stretch and its ability to adsorb to gold as well as coordinate with deprotonated sulfonate groups in EPPS as shown in Fig. 4A. Because gold nanostars begin to restructure in acidic solutions,[30] gold nanostars were activated briefly in an acidic solution before uranyl was added. Reaction conditions were selected so that the LSPR properties of the nanostars did not change

significantly (i.e., $\lambda_{max,2}$ did not shift more than 3 nm and no visible changes in the other two extinction features). In so doing, reproducible SERS signals are observed and reported here.

Previously, we demonstrated that carboxylated gold nanostars yield SERS signals for uranyl that scale with uranyl concentration,[27] and similar results are possible for gold nanostars with a given morphology. To focus on morphology implications only, representative SERS spectra for 40 μM uranyl incubated with gold nanostars with varying branch lengths are shown in Fig. 4B. Gold nanostars were diluted to a final optical density of 0.6 at $\lambda_{max,2}$ (see Fig. 2B) for consistency. This results in nanostars concentrations of 0.87, 0.54, 0.38, and 0.31 pM for Fig. 3B-1 to 3B-4, respectively. Only data in the uranyl spectral window are shown. Four spectral features are noted. The two lowest wavenumber modes centered at 825 and 800 cm^{-1} and are associated with EPPS (C-H deformation modes).[44] The vibrational features centered at 870 and 843 cm^{-1} are attributed to the U-O symmetric wavenumber for uranyl directly adsorbed to gold and via sulfonate coordination (see detailed structure in Fig. 4A), respectively. For clarity, the most abundant species of uranyl cations[45] and EPPS[30] at pH 3-4 are shown. Upon incubation, sulfonate is hypothesized to coordinate to uranyl via monodentate (9 cm^{-1} red shift) and bidentate (18 cm^{-1} red shift) geometries. These shifts are calculated with respect hydrated uranyl (~870 cm^{-1})[46] and estimated from impacts from sulfate[47] and carboxylate[48] coordination. Of note, SERS signals associated with uranyl increase with increasing aspect ratio of the nanostars by ~1100, 1800, and 2200%, a result that cannot be attributed to an increase in the number of molecules bound to the branches alone (surface area per branch increases by ~15, 170, and 270% relative to the raspberry-like structures, respectively).

Furthermore and as shown in Fig. 4C, the vibrational mode associated with uranyl directly interacting with gold remains approximately constant while the sulfonate coordinated species increases systematically. We attribute these spectral changes to variations in gold nanostar morphology and their resulting plasmonic properties near the excitation wavelength. Because an increase in radius of curvature of the tips of the nanostar branches[11] as well as a decrease in nanostar concentration should cause SERS intensities to decrease,[49] the observed systematic and reproducible increase in SERS magnitude likely depends on branch morphology (i.e., length and aspect ratio) and as a result improved plasmonic properties for SERS enhancement. Namely, as branch aspect ratio (and length) increases, electromagnetic enhancement associated the bonding (i.e., bright) plasmonic mode becomes more favorable, and plasmonic contributions arising from branch-branch coupling is promoted thereby increasing the overall SERS signal observed for uranyl through dark plasmon mode[20,36,50] excitation. Because radiative losses are less at these spectral regions (vs. on or near a bright resonance), SERS signals increase. As a result, this study highlights the combined importance of the plasmonic properties as well as morphology of gold nanostars in promoting SERS signals associated with small molecule detection.

4 | CONCLUSIONS

In conclusion, the importance of both gold nanostar morphology and plasmonic properties are demonstrated for the SERS detection of uranyl. By varying the concentration of the reducing and stabilizing agent EPPS during synthesis, LSPR spectra with up to three resonances were observed. The two plasmonic features that were observed in the visible region of electromagnetic spectrum were attributed to hybridization between the nanostar core and branches. The third

resonance, which was tunable and in the near infrared region of the spectrum grew in magnitude as branch length increased and arose because of branch-branch coupling. These spectral features were correlated with an increase in the length and aspect ratio of the nanostar branches. The stabilizing agent, EPPS, served a third purpose as well. This was to promote uranyl capture and SERS detection. It was demonstrated that gold nanostars with the longest branches and aspect ratios gave rise to the largest SERS signals. This enhancement was attributed to the ideal plasmonic properties of the nanostars for excitation at near infrared wavelengths. In the future, similar effects could be exploited for other trace molecular detection using gold nanostars.

ACKNOWLEDGEMENTS
This work is supported by the National Science Foundation, (CHE-1707859, nanostar synthesis) and the National Institute of Environmental Health Sciences of the National Institutes of Health (R01ES027145, SERS detection of uranyl). We thank Grace Lu for collecting some TEM images as well as Grace Lu and Binita Neupane for collecting some SERS spectra.

CONFLICT OF INTEREST
The authors declare no financial or commercial conflict of interest.

ORCID
Amanda J. Haes. orcid.org/0000-0001-7232-6825
Rachel Harder. orcid.org/0000-0003-2165-3898
Lahiru Wijenayaka. orcid.org/0000-0001-6788-9981
Hoa Phan. orcid.org/0000-0002-0793-8822

REFERENCES

[1] X. Xia, J. Zeng, B. McDearmon, Y. Zheng, Q. Li, Y. Xia, *Angew. Chem.* **2011**, *50*, 12542.
[2] R. P. M. Holler, C. Kuttner, M. Mayer, R. Wang, M. Dulle, R. Contreras-Caceres, A. Fery, L. M. Liz-Marzan, *ACS Photonics* **2020**, *7*, 1839.
[3] A.-I. Henry, J. M. Bingham, E. Ringe, L. D. Marks, G. C. Schatz, R. P. Van Duyne, *J. Phys. Chem. C* **2011**, *115*, 9291.
[4] J. Jiang, L. Ma, J. Chen, P. Zhang, H. Wu, Z. Zhang, S. Wang, W. Yun, Y. Li, J. Jia, J. Liao, *Microchim. Acta* **2017**, *184*, 2775.
[5] I. Haidar, G. Lévi, L. Mouton, J. Aubard, J. Grand, S. Lau-Truong, D. R. Neuville, N. Félidj, L. Boubekeur-Lecaque, *PCCP* **2016**, *18*, 32272.
[6] J. Cao, T. Sun, K. T. V. Grattan, *Sensors Actuat. B-Chem.* **2014**, *195*, 332.
[7] C.-C. Huang, C.-H. Huang, I. T. Kuo, L.-K. Chau, T.-S. Yang, *Colloids Surf. A: Physicochem. Eng. Asp.* **2012**, *409*, 61.
[8] M. Bhamidipati, L. Fabris, *Bioconjugate Chem.* **2017**, *28*, 449.
[9] J. Cai, V. Raghavan, Y. J. Bai, M. H. Zhou, X. L. Liu, C. Y. Liao, P. Ma, L. Shi, P. Dockery, I. Keogh, H. M. Fan, M. Olivo, *J. Mater. Chem. B* **2015**, *3*, 7377.
[10] A. Y. F. Mahmoud, C. J. Rusin, M. T. McDermott, *Analyst* **2020**, *145*, 1396.
[11] X. Meng, J. Dyer, Y. Huo, C. Jiang, *Langmuir* **2020**, *36*, 3558.
[12] M. Bhamidipati, H.-Y. Cho, K.-B. Lee, L. Fabris, *Bioconjugate Chem.* **2018**, *29*, 2970.
[13] J. A. Webb, W. R. Erwin, H. F. Zarick, J. Aufrecht, H. W. Manning, M. J. Lang, C. L. Pint, R. Bardhan, *J. Phys. Chem. C* **2014**, *118*, 3696.

[14] P. S. Kumar, I. Pastoriza-Santos, B. Rodríguez-González, F. J. G. d. Abajo, L. M. Liz-Marzán, *Nanotechnology* **2008**, *19*, 015606.
[15] C. G. Khoury, T. Vo-Dinh, *J. Phys. Chem. C* **2008**, *112*, 18849.
[16] H. Yuan, C. G. Khoury, C. M. Wilson, G. A. Grant, A. J. Bennett, T. Vo-Dinh, *Nanomedicine: Nanotechnology, Biology and Medicine* **2012**, *8*, 1355.
[17] R. Rodríguez-Oliveros, J. A. Sánchez-Gil, *Opt. Express* **2012**, *20*, 621.
[18] C. Hrelescu, T. K. Sau, A. L. Rogach, F. Jäckel, J. Feldmann, *Appl. Phys. Lett.* **2009**, *94*, 153113.
[19] J. M. Hoffmann, X. Yin, J. Richter, A. Hartung, T. W. W. Maß, T. Taubner, *J. Phys. Chem. C* **2013**, *117*, 11311.
[20] L. V. Brown, K. Zhao, N. King, H. Sobhani, P. Nordlander, N. J. Halas, *J. Am. Chem. Soc.* **2013**, *135*, 3688.
[21] A. Habib, M. Tabata, Y. G. Wu, *Bull. Chem. Soc. Jpn.* **2005**, *78*, 262.
[22] J. Xie, J. Y. Lee, D. I. C. Wang, *Chem. Mater.* **2007**, *19*, 2823.
[23] K. Chandra, K. S. B. Culver, S. E. Werner, R. C. Lee, T. W. Odom, *Chem. Mater.* **2016**, *28*, 6763.
[24] H. Liu, Y. Xu, Y. Qin, W. Sanderson, D. Crowley, C. H. Turner, Y. Bao, *J. Phys. Chem. C* **2013**, *117*, 17143.
[25] L. S. Jung, C. T. Campbell, *J. Phys. Chem. B* **2000**, *104*, 11168.
[26] S. Gabor *Introduction to Surface Chemistry and Catalysis*, 1994.
[27] G. Lu, T. Z. Forbes, A. J. Haes, *Analyst* **2016**, *141*, 5137.
[28] G. Lu, A. J. Johns, B. Neupane, H. T. Phan, D. M. Cwiertny, T. Z. Forbes, A. J. Haes, *Anal. Chem.* **2018**, *90*, 6766.
[29] H. de Puig, J. O. Tam, C.-W. Yen, L. Gehrke, K. Hamad-Schifferli, *J. Phys. Chem. C* **2015**, *119*, 17408.
[30] W. Xi, A. J. Haes, *J. Am. Chem. Soc.* **2019**, *141*, 4034.
[31] G. Lu, T. Z. Forbes, A. J. Haes, *Anal. Chem.* **2016**, *88*, 773.
[32] G. Lu, A. J. Haes, T. Z. Forbes, *Coord. Chem. Rev.* **2018**, *374*, 314.
[33] C. Gullekson, L. Lucas, K. Hewitt, L. Kreplak, *Biophys. J.* **2011**, *100*, 1837.
[34] F. Le, D. W. Brandl, Y. A. Urzhumov, H. Wang, J. Kundu, N. J. Halas, J. Aizpurua, P. Nordlander, *ACS Nano* **2008**, *2*, 707.
[35] E. S. Kooij, W. Ahmed, C. Hellenthal, H. J. W. Zandvliet, B. Poelsema, *Colloids Surf. A Physicochem. Eng. Asp.* **2012**, *413*, 231.
[36] F. Hao, C. L. Nehl, J. H. Hafner, P. Nordlander, *Nano Lett.* **2007**, *7*, 729.
[37] G. Chirico, P. Pallavicini, M. Borzenkov In *Gold Nanostars: Synthesis, Properties and Biomedical Application*; Springer International Publishing: Cham, 2015, p 25.
[38] K. Chandra, V. Kumar, S. E. Werner, T. W. Odom, *ACS Omega* **2017**, *2*, 4878.
[39] T. K. Lee, S. K. Kwak, *J. Phys. Chem. C* **2014**, *118*, 5881.
[40] F. Hao, Y. Sonnefraud, P. V. Dorpe, S. A. Maier, N. J. Halas, P. Nordlander, *Nano Lett.* **2008**, *8*, 3983.
[41] J. B. Herzog, M. W. Knight, Y. Li, K. M. Evans, N. J. Halas, D. Natelson, *Nano Lett.* **2013**, *13*, 1359.
[42] F. Liu, X. Zhang, Y. Mu, J. Lin, M. Wang, H. Ma, *Adv. Opt. Mater.* **2020**, Early View (DOI:10.1002/adom.202000544).
[43] C. J. Orendorff, L. Gearheart, N. R. Jana, C. J. Murphy, *PCCP* **2006**, *8*, 165.
[44] K. Mizuoka, Y. Ikeda, *Progress in Nuclear Energy* **2005**, *47*, 426.

[45] Y. Xie, C. Chen, X. Ren, X. Wang, H. Wang, X. Wang, *Prog. Mater Sci.* **2019**, *103*, 180.
[46] M. Gál, P. L. Goggin, J. Mink, *J. Mol. Struct.* **1984**, *114*, 459.
[47] C. Nguyen Trung, G. M. Begun, D. A. Palmer, *Inorg. Chem.* **1992**, *31*, 5280.
[48] F. Quilès, A. Burneau, *Vib. Spectrosc* **1998**, *18*, 61.
[49] A. D'Hollander, E. Mathieu, H. Jans, G. Vande Velde, T. Stakenborg, P. Van Dorpe, U. Himmelreich, L. Lagae, *Intern. J.Nanomedicine* **2016**, *11*, 3703.
[50] D. E. Gómez, Z. Q. Teo, M. Altissimo, T. J. Davis, S. Earl, A. Roberts, *Nano Lett.* **2013**, *13*, 3722.

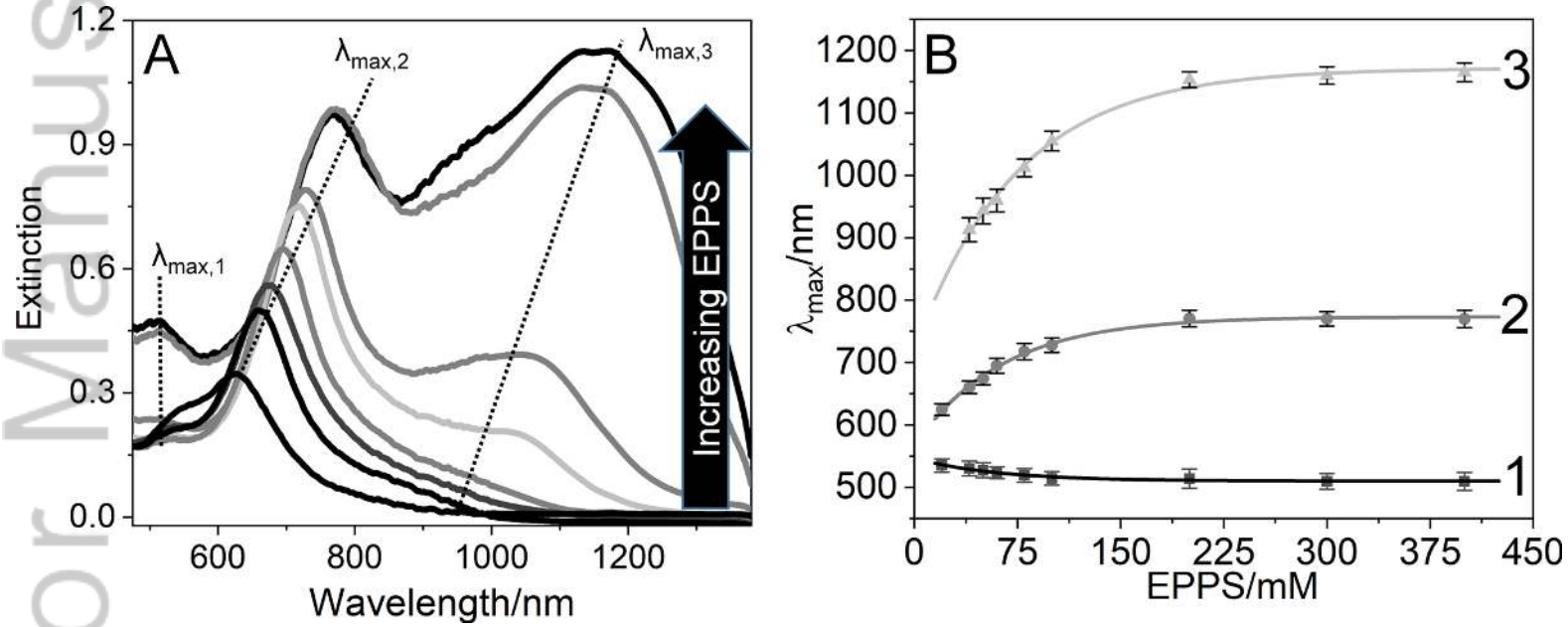

JRS_5994_Figure 1.tif

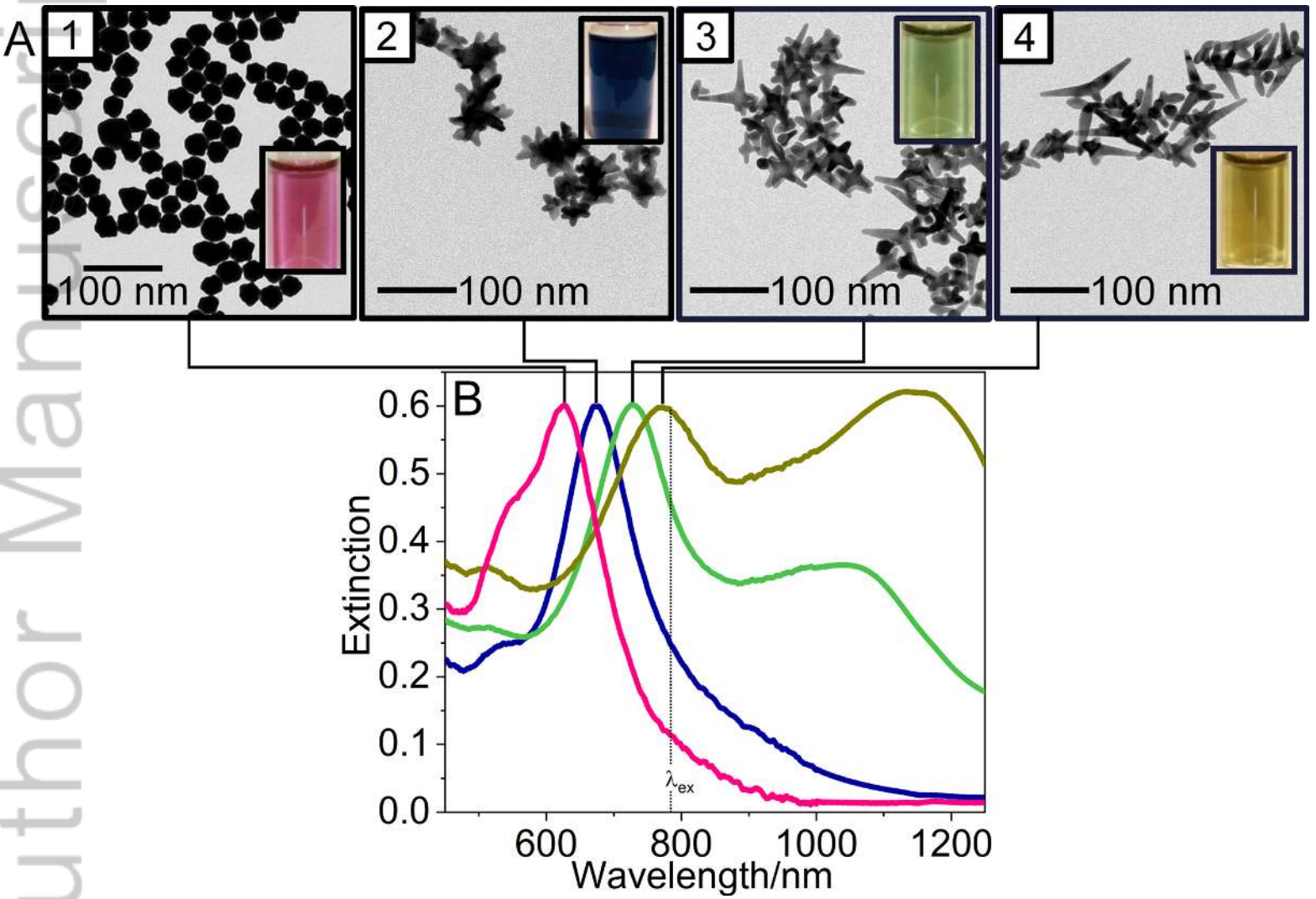

JRS_5994_Figure 2.tif

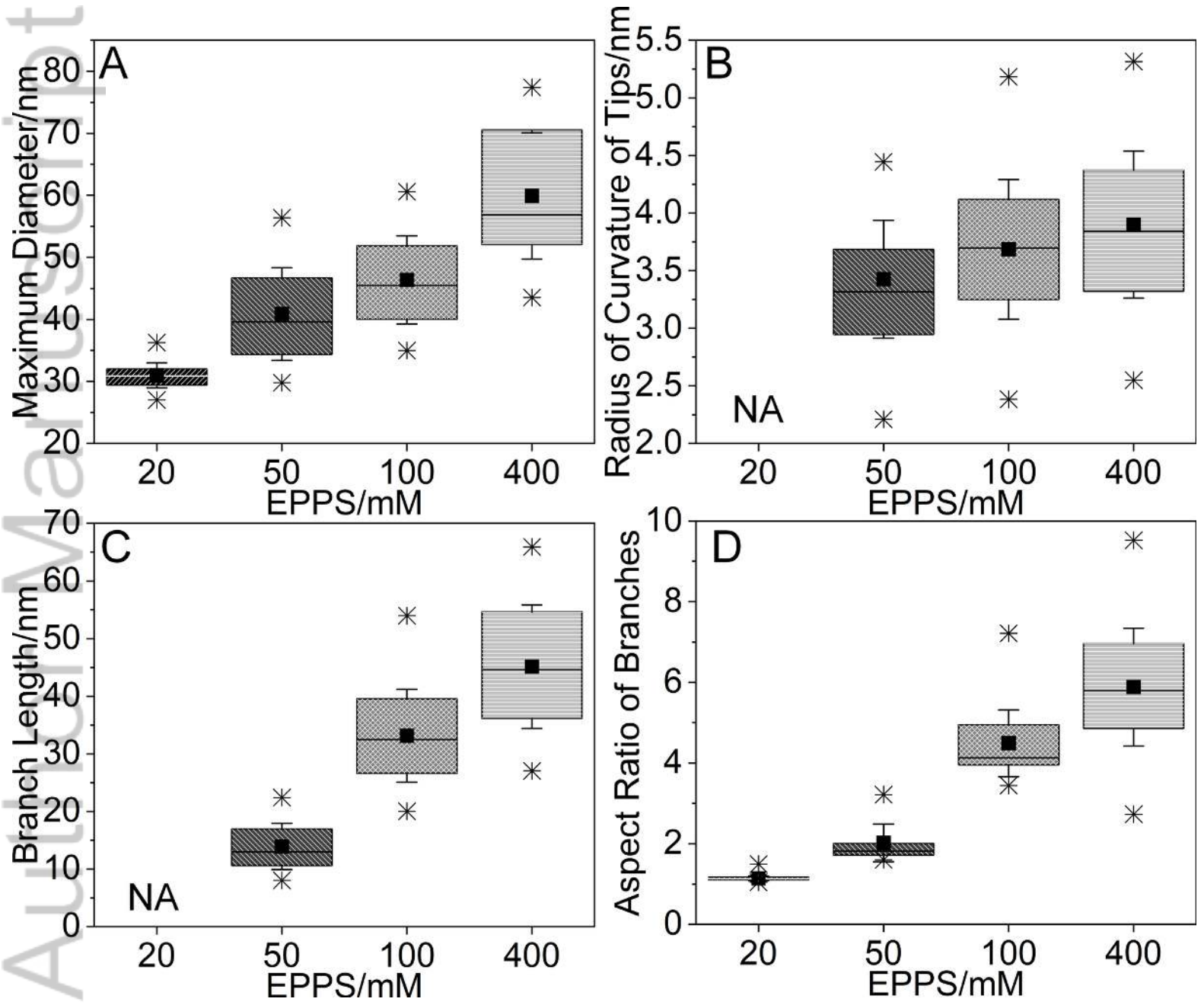

JRS_5994_Figure 3.tif

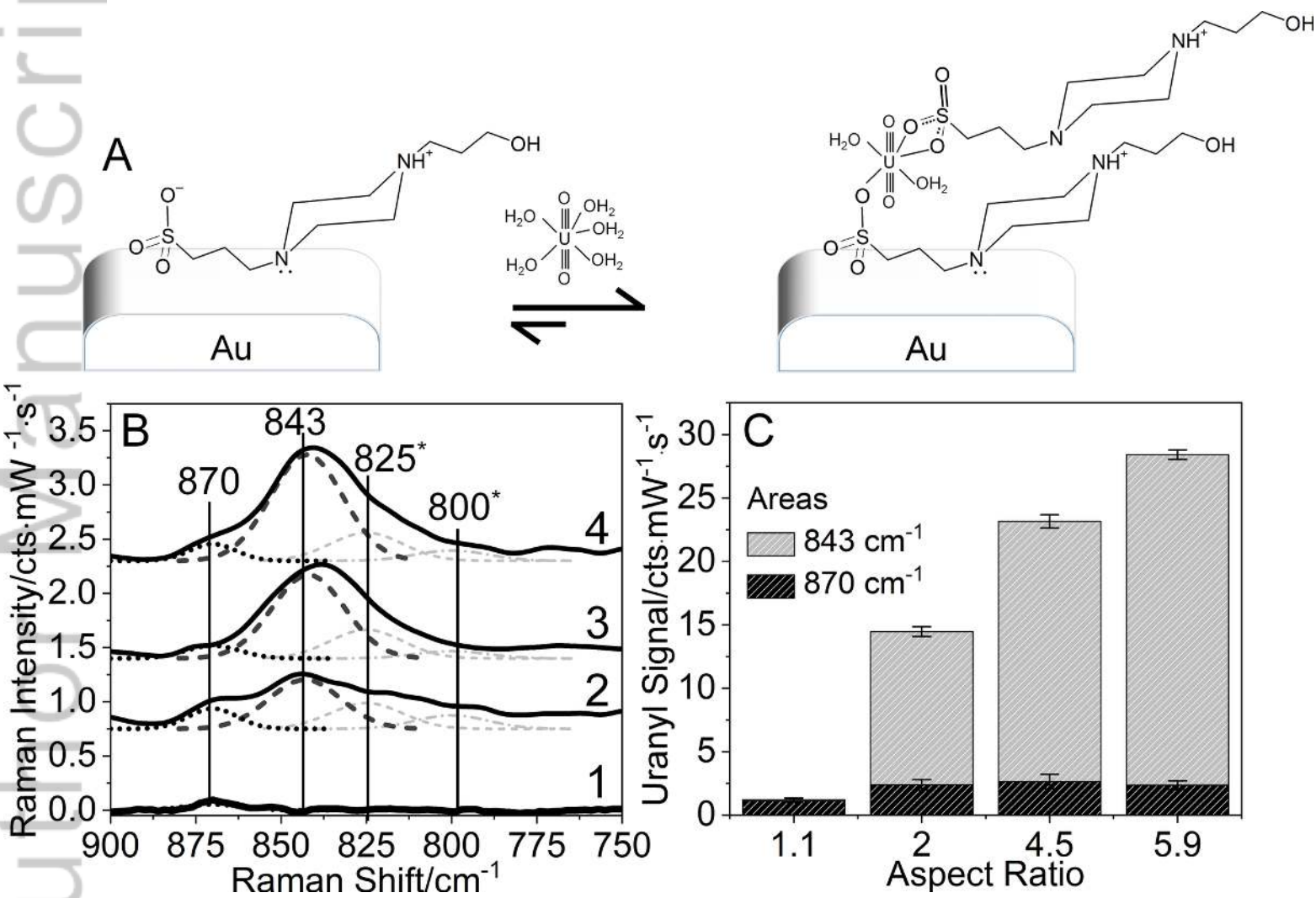

JRS_5994_Figure 4.tif